LES simulation for evaluatio of acoustic response of subcritical coaxial flames submitted to High-Frequency acoustic fields

Aurélie Nicole, Luc-Henry Dorey, Lucien Vingert, Marie Théron

LES SIMULATION FOR EVALUATION OF ACOUSTIC RESPONSE OF SUBCRITICAL COAXIAL FLAME SUBMITTED TO HIGH-FREQUENCY ACOUSTIC FIELDS

SPACE PROPULSION 2020

ESTORIL, PORTUGAL / 08 – 12 FEBRUARY 2021

Aurelie NICOLE [(1)], Luc-Henry DOREY [(1)], Lucien VINGERT [(1)], Marie THERON [(2)]

[(1)] DMPE, ONERA,
Université Paris Saclay,
F-91123 Palaiseau,
FRANCE
Tel. : +33 1 80 38 60 38
Email : aurelie.nicole@onera.fr:
[(2)]CNES - Direction des Lanceurs
52 rue Jacques Hillairet
75012 Paris Cedex
FRANCE

KEYWORDS: HF, COMBUSTION INSTABILITIES, NUMERICAL SIMULATION

ABSTRACT:

Since the beginning of the space race, high-frequency instabilities have been one of the major issues of liquid rocket engines development and qualification. In order to investigate the acoustic response of cryogenic flames to high-frequency acoustic fields, experimental campaigns have been carried out on the MASCOTTE test bench, during which the chamber was supplied with five Lox/Methane coaxial injectors and was equipped with the Very High Amplitude Modulator (VHAM) to generate acoustic excitation. This paper presents LES simulations of one subcritical operating point of the MASCOTTE-VHAM test campaign performed in the frame of ONERA/CNES joint research program on high-frequency instabilities. The response of the chamber to several acoustic modulations was studied. The simulations show that the flames response is maximized for a modulation corresponding to the 1T1L chamber eigenmode. In this case, the liquid core length is drastically reduced, the atomization and the combustion are enhanced.

1. INTRODUCTION

Cryogenic propellant rocket engines power most modern space launchers [1] and since the beginning of the space race, high-frequency (HF) instabilities have been one of the major issues of liquid rocket engines development and qualification. Their consequences are often serious as they can lead to engine destruction [2,3]. Competition from new private players is pushing manufacturers to reduce the development and implementation costs of their rockets. Recent innovations tend to increase the risk of instability in the operating regime of the engines, like the use of methane instead of hydrogen [4,5]. To investigate these instabilities, the effect of methane use and the extension of operating domains for reusable rocket engines, ONERA has followed two axis: an experimental one with tests performed in representative operating conditions at MASCOTTE test rig [6] and a numerical one with Computational Fluid Dynamics (CFD) simulations performed with CEDRE, the ONERA in-house CFD tool [7]. The strong synergy between simulation and experimentation helps for models validation and for better understanding of phenomena at stake.

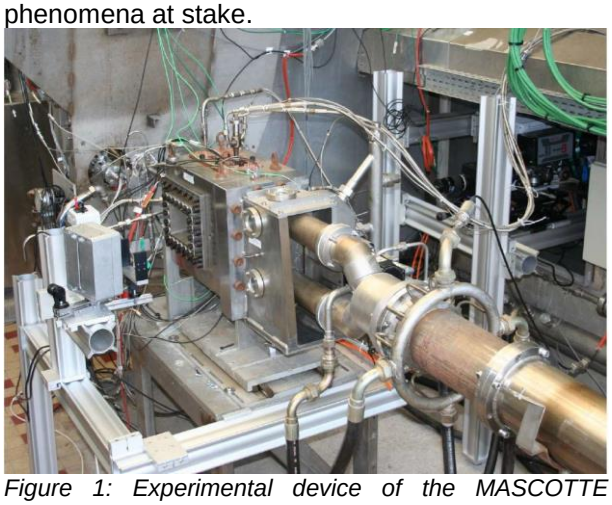

Figure 1: Experimental device of the MASCOTTE chamber equipped with VHAM

Several HF experimental campaigns were carried out on the MASCOTTE test bench. This paper will focus on the campaign where the instabilities were

generated by the Very High Amplitude Modulator (VHAM) [8]. In this configuration, the MASCOTTE chamber was fed by five Lox/Methane coaxial injection elements and was equipped with the VHAM in order to generate transverse acoustic excitation within the chamber (Figure 1). The amplitudes are representative of those found in actual engines undergoing HF instabilities, up to 20% of the chamber mean pressure. Several operating points were studied from a pressure of 10 bar up to 70 bar, so that all LOx injection conditions were covered, both subcritical and transcritical.

As transcritical operating points were already investigated [9], computation reported in this article focuses on a subcritical operating point. Many physical phenomena are at stake in this subcritical operating point, such as atomization, evaporation, but also combustion and turbulence. So, we proceeded step-by-step in order to gradually make our simulations more complex and to have sufficient confidence in each step. After having simulated steady reactive flow [10] in subcritical condition, the effect of acoustic modulation was investigated on an air-assisted liquid jet [11]. Based on these two successful simulations, the coupling between acoustic, two-phase flow and combustion was investigated in details with a single injector reactive test case first. Then we carried out the full simulation of the VHAM subcritical operating point of MASCOTTE reduced-scale experiment. This paper will essentially expose the simulations for the latter, in addition to a more detailed analysis proceeded on the mono-injector case thanks to faster restitution times.

First, the numerical configuration was described by giving few words about the experimental setup, the physical and numerical models and the grid. The subcritical methodology was illustrated and the numerical experiment is presented. In a second paragraph, the steady simulation is investigated in detail. Then we proposed an assessment of the VHAM simulation method. Finally, the simulation of the VHAM case will be performed with 3 different frequency modulations. Their effect on the liquid core and combustion will be analysed in detail on the experimental test case.

2. NUMERICAL CONFIGURATION

2.1. Experimental setup

The chosen operation point corresponds to subcritical conditions. The expected pressure in the chamber is 26 bar. This chamber is supplied by a row of five injection units set in the vertical plane of symmetry (see [8] for a schematic view). It is a rectangular section box, 5 times higher and 7 times longer than it is wide. The injectors used are coaxial injectors. Liquid oxygen is injected in the centre and gaseous methane at the periphery. Large lateral portholes provide a view of the flame as well as the collective effects of the injectors. These portholes are cooled by a helium film which, for reasons of mesh simplification and calculation, is not taken into account in the present simulations. Unsteady pressure signals are recorded by five sensors located in the chamber and two in the injection head. Table 1 summarizes the operating conditions: pressure, mass flow rates, MR the mixture ratio and J the momentum flux ratio. In the whole paper, the subscript letter F designate the methane, O the oxygen and CH, the chamber.

P_{CH} (bar)	MR (-)	J (-)
26	1.33	2

Table 1. Operating conditions

Where $\dot{m}$ is the mass flow rate, P the pressure and

$$MR = \frac{\dot{m}_O}{\dot{m}_F} \qquad \text{Eq. 1}$$

$$J = \frac{\rho_F U_F^2}{\rho_O U_O^2} \qquad \text{Eq. 2}$$

Concerning the VHAM device, it consists of a rotating toothed wheel that alternatively closes the two nozzles. One nozzle is shut when the other one is open. As a result, the gas is periodically ejected through one or other of the nozzles, generating excitation of the tangential modes, the most dangerous eigenmode for HF instabilities. The methodology for simulating the operation of the VHAM will be set out in paragraph §4. Subsequently, this case will be referred to as VHAM test case.

2.2. Physical models and numerical schemes

The simulations are performed with the in-house ONERA's code CEDRE, an unstructured compressible simulation code using finite volume method for multi-physics simulations. The fields of application are energetics and propulsion for industrial and research investigations. CEDRE provides high-fidelity CFD with massively parallel processing. It is divided in several solvers: compressible reactive flow, Lagrangian dispersed phase, Eulerian dispersed phase, radiative transfer, conduction and so on. Thus, each phenomenon can be modelled by the appropriate solver. CEDRE can perform multi-phase flow simulations with both LES or RANS approach.

The simulations of this paper are performed with LES formalism with a Smagorinsky subgrid-scale model [16]. The strategy of the multi-phase flow simulation is presented in [17]. It is based on the coupling of a separated phases solver with a dispersed phase solver to describe the size-wide two-phase flow topology. The former used a 4-equation diffuse interface model to solve on the mesh the gas and the biggest liquid structures, whereas the latter describes the spray, consisting of

spherical droplets, using an Eulerian approach based on the transport of Number Density Function moments. The size distribution is described by a sectional method with affine reconstruction. For this first simulation, 3 sections were used.
The ideal gas law provides the compressible Navier-Stokes system closure and the compressible liquid law for the liquid phase [17]. Concerning the approximation of the convective fluxes, upwind numerical fluxes based on approximate Riemann solvers with the HLLC flux scheme are used [18]. Second-order multislope MUSCL reconstructions extended to general unstructured grids are computed on each grid faces [19]. For time integration, the one-step implicit scheme is used for the steady simulation and a two-step implicit Runge-Kutta scheme for the modulated simulation.

The combustion modelling is based on relaxation to equilibrium. It is same principle as Spalding [20] and Magnussen [21] models and more recently Schmitt model [22]. [23] gives more detail about this model. The reacting rate $\dot{\omega}$ of the species i is determined by:

$$\bar{\omega}_i = \rho\, min(C f_T; f_{max})\left(Y_{i,eq} - Y_i\right)H\left(T - T_{inf}\right) \quad \text{Eq. 3}$$

This reacting rate is driven by a turbulent mixing time scale through the turbulent frequency f_T and a user constant C. ρ is the density, Y the mass fraction. The subscript *eq* is relative to the equilibrium. T is the temperature and T_{inf} is the ignition temperature. Unlike Spalding and Magnussen's model, it is not limited by the reactants disappearance of the global reaction, it is restricted by the local thermodynamic equilibrium and it takes into account radicals.

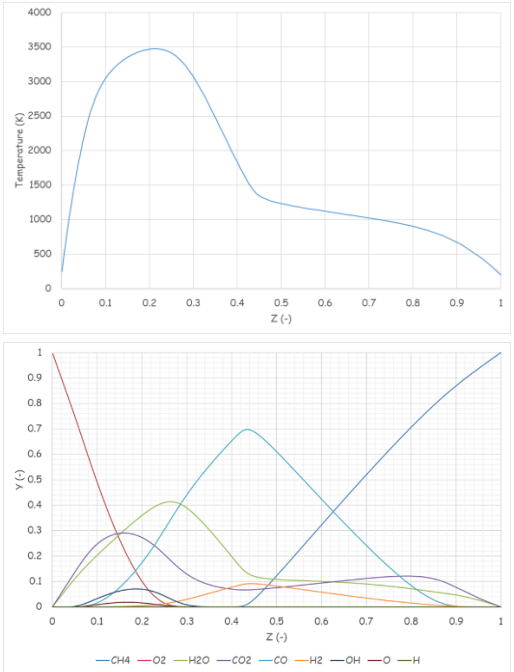

Figure 2. Evolution with Z of temperature and of the different mass fractions of the predominant species

Cantera [24] software tools were used to compute the equilibrium composition of an adiabatic flame and the flame velocity in order to determine the predominant species to represent correctly the LOx/methane combustion without too prohibitive simulation costs. For the VHAM simulation, the following species will be taken into account: CH_4, O_2, CO_2, H_2O, CO, OH, H_2, H and O. Figure 2 shows the evolution of the temperature and of the mass fractions of the chosen species as a function of the mixing fraction Z :

$$Z = \frac{sY_F - Y_O + 1}{s + 1} \quad \text{Eq. 4}$$

s is the stoichiometric mixture ratio and it is equal to 4 for O_2/CH_4 combustion. Z is 0.2 at stoichiometry.

2.3. Methodology

The methodology is represented in Figure 3. The oxygen liquid core and the biggest liquid ligaments are computed by the separated phases solver. The primary atomization of the big structures provides the oxygen droplet distribution for the dispersed phase solver. The spray is then evaporated and gives to the Navier-Stokes solver the concentration of gaseous oxygen which can burn with the methane. In case of high concentration of droplets or when droplets impact the jet, dispersed phase feeds the separated phases (impingement). Each phenomenon (atomization, evaporation, combustion and turbulence) has its own modelling and set of parameters, as it was described in the previous section.

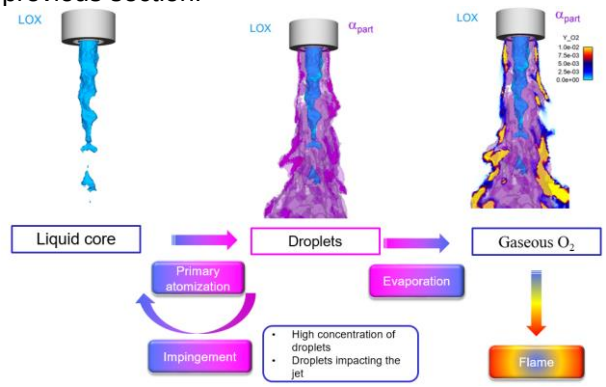

Figure 3. Computation methodology

2.4. Mesh of the VHAM configuration

Even more than in the case of steady simulations, the mesh of this acoustic simulation covers a wide range of length scales. Indeed, on the one hand, the chamber must be completely meshed to correctly represent the acoustics. On the other hand, the correct simulation of the five cryogenic flames requires the representation of very small characteristic scales. For example, the shear layer linked to the physical and geometrical features of the injectors must be finely meshed. And, the mesh must also be compatible with the power of the computers available at ONERA. As this chamber is particularly large, this can lead to a huge mesh size.

In a first approach, we chose to use a mesh compatible with the good representation of the acoustics but slightly coarse for the turbulent flow close to the injectors in order to validate the different simulation methods and to verify the behavioural trends of cryogenic flames under a transverse acoustic forcing. This mesh consists of 2.5 million tetrahedral elements. The most refined zone is located in the injector and closely downstream around the lip of each injector as shown in Figure 4. This lip is meshed by three elements along its thickness.

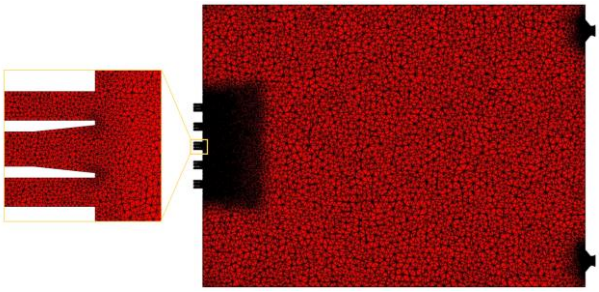

Figure 4. Cross-section of the grid and zoom on the injector part

It is a first step in the global strategy of the subcritical VHAM simulation. It allows to evaluate all the models used and to identify the first trends. A more detailed analysis of the various phenomena will be carried out on the purely numerical single-injector test case.

2.5. Single injector configuration

The simulation of this injector immersed in an acoustic field serves as a numerical experiment. The objective is to investigate in detail the interaction between acoustic / atomization / evaporation and combustion. Through this numerical test case, we want to free ourselves from a costly comparison between experiment and simulation. The operating conditions are similar to real ones but the simplicity of the case induces quick calculation feedbacks and allows assessing the methodology of the 2-phase flow simulation in the case of HF instabilities from the behaviour and robustness point of view. Comparing to the VHAM test case, the coaxial injector has thickened lips and no chamfer to generate a less costly mesh. The injector is set in intensity anti-node to maximize the diversity of acoustic effects on the liquid phase [11] as shown in Figure 5.

In order to generate a standing wave whose intensity anti-node is situated on the longitudinal axis of the injector, two waves propagated from the two lateral boundaries are superimposed. The right boundary condition is a velocity antinode and the left one is a pressure antinode:

$$\begin{cases} P_{right} = \bar{P} + \Delta P sin(2\pi f t) \\ P_{left} = \bar{P} - \Delta P cos(2\pi f t) \end{cases} \qquad \text{Eq. 5}$$

$\bar{P}$ is the mean pressure, ΔP is the amplitude of the pressure oscillations and f the modulation frequency.

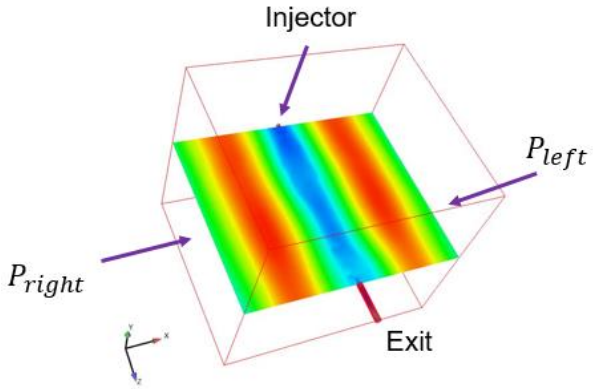

Figure 5. Single injector configuration with pressure field

For this configuration, two grids were used a coarse one and a fine one. Table 2 gives the description of these grids:

Mesh	Number of cells (M)	Cells / lip
Coarse	7.5	3
Fine	19.5	10

Table 2. Grid description

3. VHAM STEADY SIMULATION

Before simulating the case with acoustic modulation, a steady-state calculation is performed. It will be the initial condition for the modulated case. For this modulated case, the gases are ejected alternately through one or the other of the nozzles. For the steady-state case, we do not wish to favour one nozzle or the other. The calculation is therefore carried out with nozzles having a throat section half the size in order to maintain the outlet flow rate and the mean pressure of the chamber. The flow field will be analysed in detail on the point of view of the liquid core and the combustion.

3.1. Liquid core

The first element analysed is the behaviour of the liquid cores. Figure 6 gives a 3D snapshot of these liquid cores in blue and a cross-section of the drop concentration field. The five cores have a similar behaviour. The liquid cores grow until the hydrodynamic instabilities are too great and tear a ligament. The liquid core's length L_D can be compared to three analytical correlations. It is dimensioned by the diameter of the Lox pitot D_l:

- Eroglu's [12] :

$$\frac{L_D}{D_l} = 0.66\, We^{-0.4} Re_l^{-0.6} \qquad \text{Eq. 6}$$

- Villermaux's [13]:

$$\frac{L_D}{D_l} = \frac{6}{\sqrt{J}} \qquad \text{Eq. 7}$$

- Leroux's [14]:

$$\frac{L_D}{D_l} = \frac{10}{J^{0.3}} \qquad \text{Eq. 8}$$

Where J is the momentum flux ratio, We the Weber number:

$$We = \frac{\rho_g \left(U_g - U_l\right)^2 D_l}{\sigma_l} \qquad \text{Eq. 9}$$

and Re_l, the liquid Reynolds number:

$$Re_l = \frac{\rho_l U_l D_l}{\mu_l} \qquad \text{Eq. 10}$$

the subscript letter l designate the liquid and g the gas. These correlations have not been formulated for fire test cases, but they do allow trends to be estimated. For the selected operating point, we obtain a length of the liquid core between $4.3D_l$ and $8.9D_l$. The simulation gives an average length for the 5 liquid core around $4.5D_l$. This value is in good agreement with the correlations. The evolution over time of the different liquid cores is not simultaneous but no asymmetry appears on average.

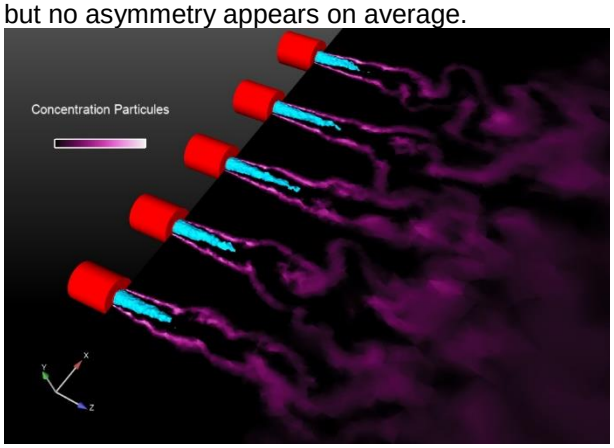

Figure 6. Liquid cores and droplet concentration

3.2. Combustion

The temperature reached in the chamber is indeed the temperature at the end of combustion for the mixing ratio of the VHAM test case, around 1500 K. This enables the computation of the chamber eigenmode. However, this maximum is not exceeded; even in the shear zones nearby the injector where we should find a temperature corresponding to stoichiometric mixture ratio around 3500 K (Cf. Figure 2).

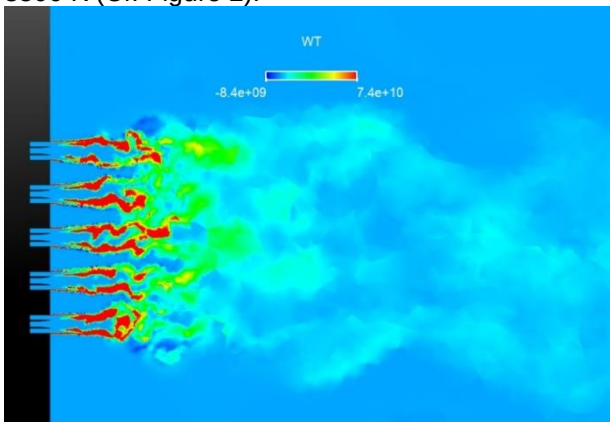

Figure 7. Heat release

Figure 7 shows an instantaneous cross-section of the heat release field. Even in the zone where the heat release is maximum, the temperature is around 1000 K.
For a better understanding of the methodology behaviour on the flame temperature, we investigate in detail the influence of key parameters in the mono-injector test case.

3.3. Influence of key parameters

In §2.3, the methodology was summarised with its several steps. In order to understand the low level of temperature in the flame, we will examine the different elements of this methodology on the mono-injector test case.
As the combustion model has been validated on gas/gas simulations, it will not be discussed here. Therefore, the vaporisation is first, examined. To enhance evaporation, the droplets diameter resulting of the atomization is divided by 10. This provides some warmed spots as shown in Figure 8, but the mixture layer remains cold.

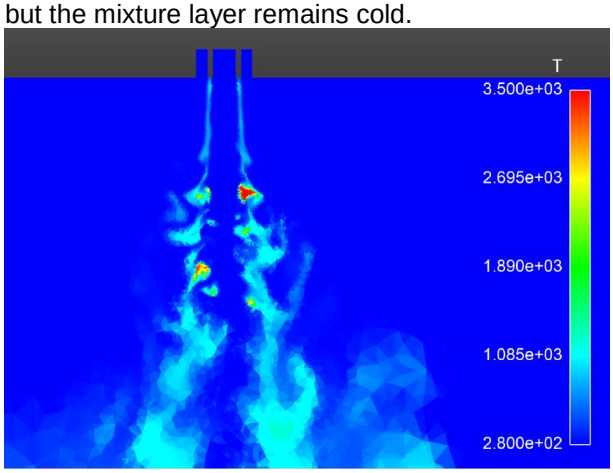

Figure 8. Temperature field in a transverse cross-section when the droplets diameter is divided by 10

It seems that the flow field close to the injector is not representative of a flame. One reason could be that the liquid core is not sufficiently destabilised and this inhibits atomization. Therefore, the atomization rate is artificially increased to see the influence on the temperature field. This rate is arbitrarily, multiplied by 3 and the result is presented in Figure 9. The temperature and the mass fraction of O_2 are significantly increased. This shows the great importance of this model, which needs to be fine-tuned. In order to do so, validation is necessary, in particular by means of experimental databases, including direct measurements like polydispersity index or indirect measurements such as precise flame characteristics since the flame is highly dependent on atomization.

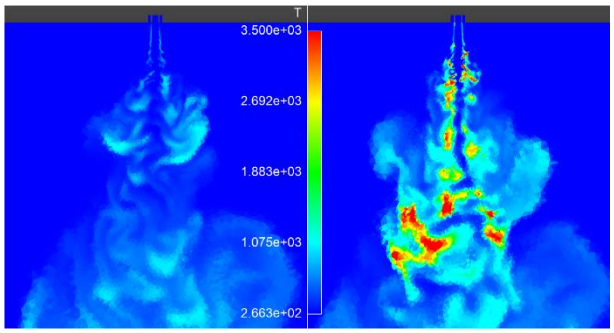

Figure 9. Temperature field in a transverse cross-section when the atomization is multiplied by 3

The refinement of the mesh is also an interesting approach because a finer mesh better describes liquid wavelengths on the liquid core. The first effect is on the liquid core and the liquid-gas interface. This interface is then destabilised much faster on the fine mesh. The wrinkling caught by the fine mesh is not comparable to that captured by the initial mesh as shown in Figure 10. This has the direct consequence of refining the liquid core, and ultimately reducing its length.
Concerning the gas phase flow, Figure 11 comparing the vorticity fields also shows the important local effect of spatial discretisation: the turbulence of the two mixing layers, that between the liquid and the gaseous coflow and that between the coflow and the external recirculation, is much better resolved on the fine mesh. The resulting mixture appears stronger in the latter case. Atomization and evaporation are enhanced with fine mesh. This leads to a different flame topology nearby the injector as it is shown in Figure 12. First, close downstream of the injector lip, the flame is better hooked up with a high heat release value contrary to the coarse mesh case. In addition, the flame develops near the new highly wrinkled zone of the liquid core and shows the direct effect of the wrinkling of the interface on combustion.

Finally, the comparison of the temperature fields obtained is shown in Figure 13. The differences in topology between the two simulation cases are similar to the vorticity fields, while the temperature levels are affected only to a lesser extent, with a maximum observed temperature of approximately 1300K for the optimised fine mesh compared to 1000K for the initial case. Finally, the fineness of the spatial discretization appears to be decisive on the reproduction of the interface wrinkling and thus on the reproduction of the flame topology. The new mesh used, designed to provide a significant gain in resolution, does not, however, make it possible to reproduce temperature levels considered sufficient for CH_4/O_2 combustion. The fineness of the mesh is therefore not the complete answer to this temperature issue.

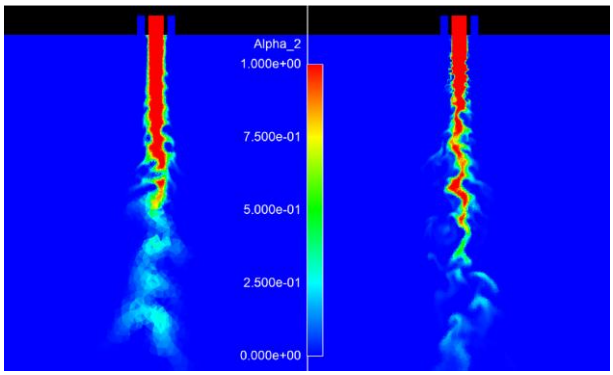

Figure 10. Instantaneous liquid volume fraction field for initial mesh (left) and fine mesh (right).

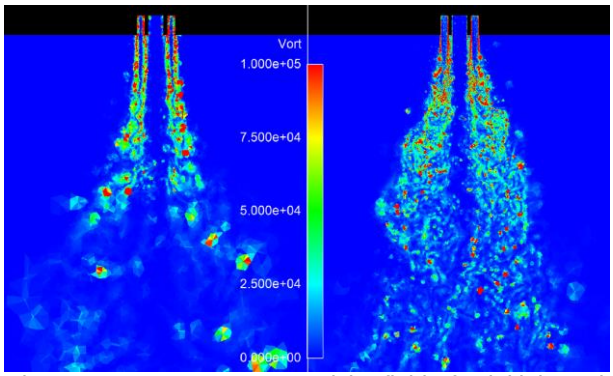

Figure 11. Instantaneous vorticity fields for initial mesh (left) and fine mesh (right).

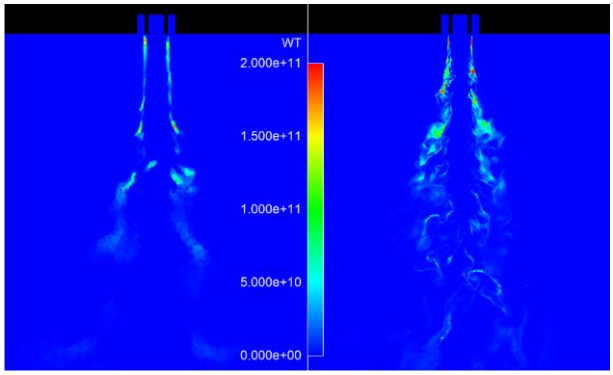

Figure 12. Instantaneous heat release for initial mesh (left) and fine mesh (right).

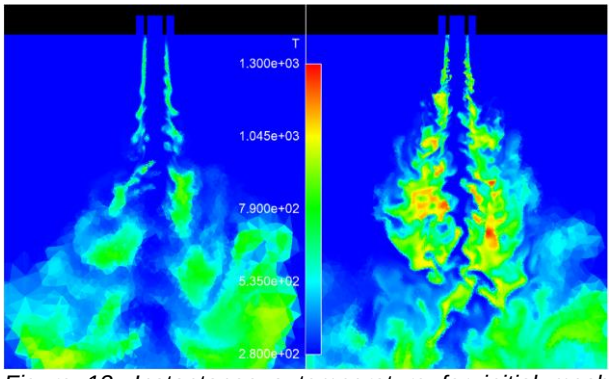

Figure 13. Instantaneous temperature for initial mesh (left) and fine mesh (right).

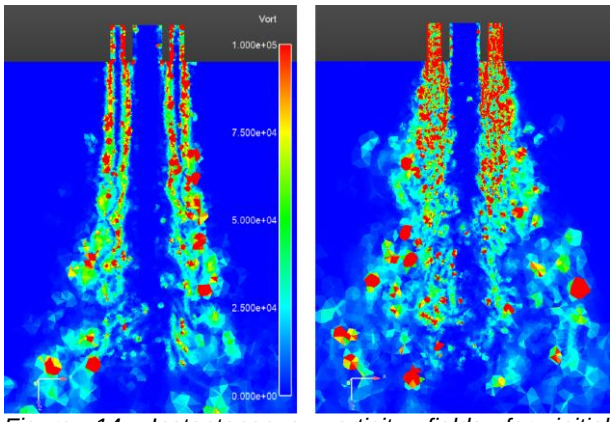

Figure 14. Instantaneous vorticity fields for initial simulation (left) and with SEM (right).

The influence of the turbulence level at the inlet was also investigated. The use of synthetic eddy method (SEM) [25] to prescribe turbulence at the inlet appears to be efficient to get correct level of turbulence in the chamber as shown in Figure 14. Turbulence is much more developed in the gaseous coflow inside the injector, and at its outlet, the turbulent fluctuations thicken the coflow, compared to the initial simulation. The consequences on the temperature field (Figure 15) are nevertheless rather limited. Turbulence increases mixing but remains limited by the amount of gaseous oxygen available.

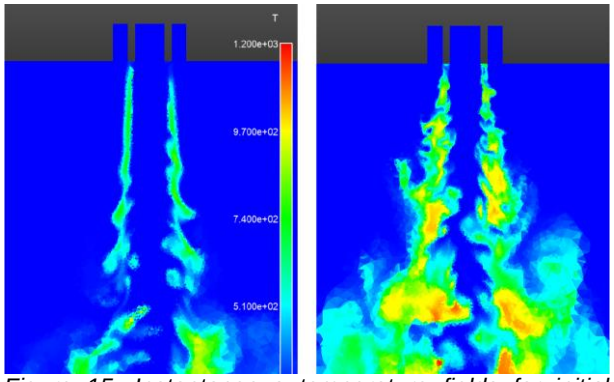

Figure 15. Instantaneous temperature fields for initial simulation (left) and with SEM (right).

Finally, the SEM appears necessary since it generates a more realistic coflow and contributes to the hanging of the flame on the injector lip. However, it alone does not increase the atomisation of the LOx sufficiently to allow a more efficient combustion.

The grid refinement and the good representation of turbulence are important for simulation of a subcritical diffusion flame. However, the primary atomisation seems to be the most important step to reproduce correct flame temperatures. Therefore, special attention must be paid to its modelling. Results of this section showed that combustion is influenced by several phenomena linked to the subcritical state of Lox, and parameters involved in corresponding models. Extended investigation of parameters influence is currently ongoing work. In particular, for this first simulation of the VHAM case, it is not realistic to envisage using such a fine mesh. The results will only allow us to identify trends, but this first step is essential in order to carry out calculations on more detailed meshes.

4. METHODOLOGY FOR VHAM SIMULATION

To simulate the alternative closure of the nozzles, a mobile mesh could have been used but would have made this already arduous simulation more complex. We therefore opted for a simulation of this closure via unsteady exit conditions. Thus, the nozzles are cut at their throttle and a periodic pressure condition is applied, as shown in Figure 16. The following conditions are therefore applied to the two outputs OUT1 and OUT2 so that their pressure signals are out-of-phase.

$$\begin{cases} P_{OUT1} = \bar{P} + \Delta P sin(2\pi f) \\ P_{OUT2} = \bar{P} + \Delta P sin(2\pi f t + \pi) \end{cases} \quad \text{Eq. 11}$$

In order to validate the method, a simulation is carried out on an equivalent chamber fed by 5 injectors delivering the combustion products at the mixing ratio of our case. The gas composition is given by a Cantera equilibrium computation. The grid of this hot gas chamber consists of 780,500 tetrahedral elements.

Figure 16. Modification of the nozzles of the MASCOTTE chamber to apply the outgoing pressure oscillations

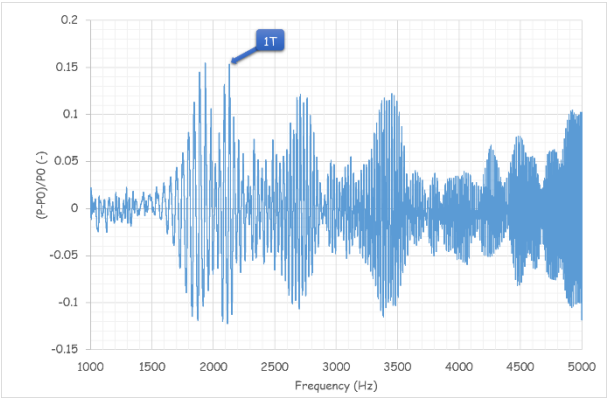

Figure 17. Pressure in the chamber for a siren test

In order to assess the chamber eigenmodes, a siren test was performed as in the experimental setup.
A first test is carried out with a frequency ramp from 1kHz to 5kHz over a period of 35 ms. The chamber pressure response is plotted in Figure 17. The

frequency of the first tangential mode is estimated around 2200 Hz.
Then, following the siren test, mono-frequency tests were carried out. Several frequencies were investigated with an excitation amplitude of 1%. When the frequency does not correspond to an eigenmode, the pressure response of the chamber remains around 1%. On the contrary, for a frequency close to the first tangential mode, the amplitude of the pressure disturbance is 12% peak-to-peak. In order to illustrate this point, Figure 18 shows the pressure evolution over one period for two frequencies: f_1 and f_2. f_1 is any frequency. It does not correspond to any eigenmode. f_2 is close to the first tangential mode. The chamber response is much more intense in the case of the excitation at frequency f_2 and the 1T mode shape is verified. This tends to validate our excitation method. We will now apply it to the complete case.

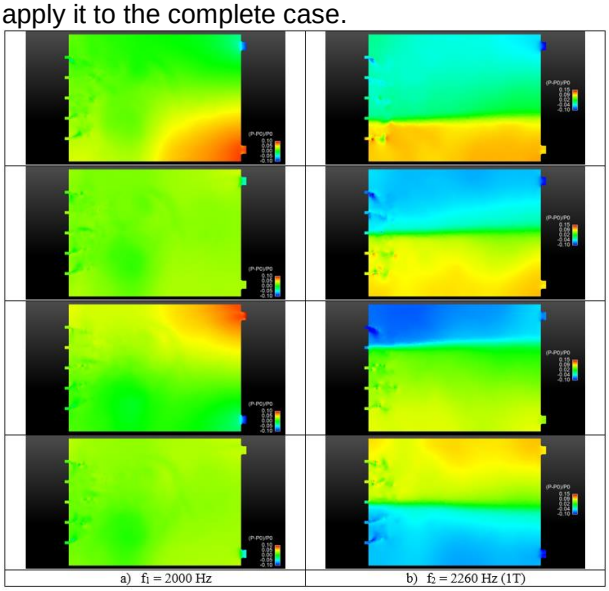

Figure 18. Comparison of the cross-section of the pressure field over one period for two frequencies.

5. ANALYSIS OF THE RESPONSE TO ACOUSTIC EXCITATION

5.1. Chamber response

As the mesh size of the complete case is 3 times larger than the hot gas mesh size and its time step is quite small due to the two-phase phenomena, a siren test to calculate the value of the first tangential mode cannot be considered.
Two cases of mono-frequency modulation have been simulated: one case at 1000 Hz which does not correspond to any natural eigenmode frequency of the chamber and another at 2200 Hz close to the theoretical eigenmode. Table 3 gives the pick-to-pick amplitude of the chamber pressure. This table shows that the closer a frequency is to a chamber natural frequency, the greater the amplitude of the chamber pressure oscillations is and it confirms the fact that the frequency of 2200 Hz corresponds to a chamber eigenmode.

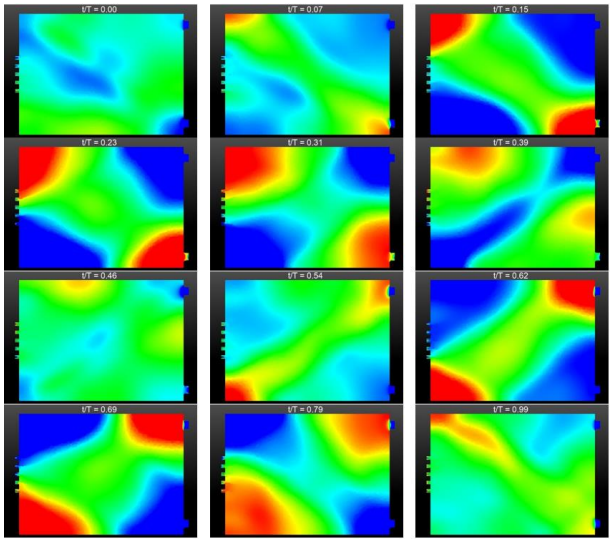

Figure 19. Pressure field in a cross-section of the chamber at different times within a period at 2200 Hz

Figure 19 gives a cross-section of the pressure field corresponding to this frequency for different times within a period. This looks like a 1T1L mode. Note that in the "hot gas" case presented in §4, the frequency of 2200 Hz corresponds to the 1T mode whereas in the VHAM case it is the 1T1L mode. As the temperature is not uniform in the VHAM case, it modifies the eigenfrequencies of the system. It is to be compared with the experimental measurements of 1T1L presented in the Méry thesis [26], which was measured at a frequency of 2340 Hz.

	Pick-to-pick amplitude of chamber pressure	Average liquid core length
Without modulation	-	$4.5D_1$
Modulation of 1000 Hz	1%	$3.5D_1$
Modulation of 2200 Hz	16%	$1.6D_1$

Table 3. Amplitude of chamber pressure and liquid core length for several modulations

5.2. Influence on the liquid core

First, we investigate the effect of modulation on the liquid core. Table 3 gives the average liquid core for the two modulations and without modulation. As for the chamber pressure response, the effect on the liquid core is maximised for the chamber eigenfrequency at 2200 Hz. Nevertheless, even a modulation at any frequency has a non-negligible effect on the length of the liquid core. Indeed, the even small pressure oscillations generate modulations of the inlet mass flow rate. And those modulations shorten the liquid core length as explained in [27]. However, the effect on the liquid core is much greater at the frequency of 2200 Hz than at the frequency of 1000 Hz. The length of the liquid core is almost divided by 3 for a modulation of 2200 Hz. This is illustrated in Figure 20 that shows the liquid volume fraction field for the modulation of 1000 Hz and the modulation of 2200 Hz.

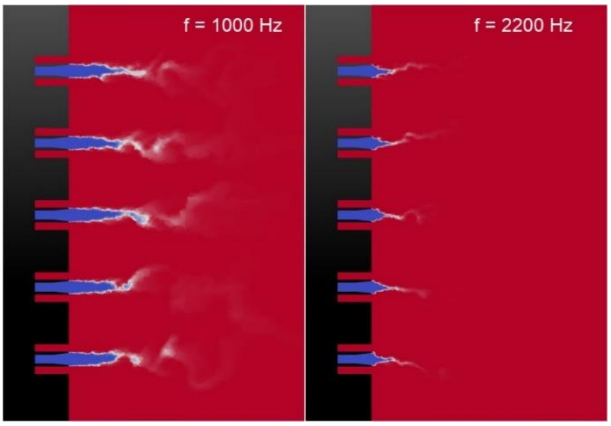

Figure 20. Instantaneous liquid volume fraction field with a modulation of 1000 Hz (left) and 2200 Hz (right).

In order to analyse in detail the effect of acoustics on the liquid core, a further study was carried out on the numerical mono-injector case. In the steady-state case, the length of the liquid core is a balance between the aerodynamic stresses exerted by the gas flow on the liquid core and the surface tension stabilising forces. In modulated cases, two phenomena upset this equilibrium: inlet flow oscillations and the acoustic radiation pressure that lead to the shortening of the liquid core. Figure 21 shows the evolution of the length in the case with acoustic excitation. Periods of growth alternate with sudden drops in liquid core length. Two periods seem to be distinguished: the first, called T_1, during which the liquid core forcibly lengthens it by almost 50% and then is suddenly destroyed. The same phenomenon appears in the case without modulation. And, then the liquid core lengthens successively about three times by only about 20%, which corresponds to the second period T_2, close to the modulation period. This is probably due to the flattening of the liquid core because of acoustic radiative effect as presented in [11].

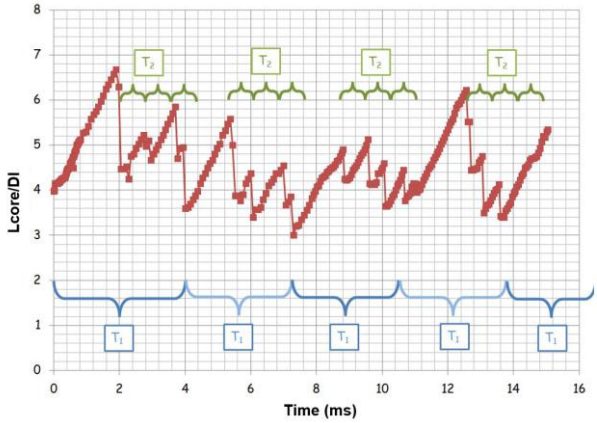

Figure 21. Evolution with time of the liquid core length

5.3. Influence on the combustion

We also investigate the effect of the acoustic modulation on the combustion. When the modulation frequency corresponds to an eigenmode of the chamber, it reinforces combustion. Temperatures of the order of 3500 K are reached in this case at 2200 Hz while they remain close to 1000 K at 1000 Hz as shown in Figure 22. The heat release (Figure 23) is also much higher. A coupling between acoustics and combustion for the eigenmodes of the chamber is therefore clearly visible.

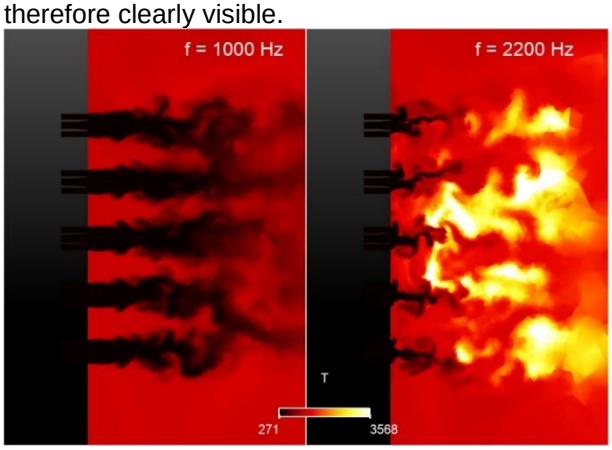

Figure 22. Instantaneous temperature field with a modulation of 1000 Hz (left) and 2200 Hz (right).

Like for the investigation of the effect of modulation on liquid core, a detail analysis was performed for the combustion with the single injector configuration. Figure 24 gives the temperature field with and without modulation for this case. The aperture angle of the flame appears to be larger in the modulated case than without modulation. This angle increases from 10° to 17°, it is almost twice as large. The flame is also shorter in the modulated test case.

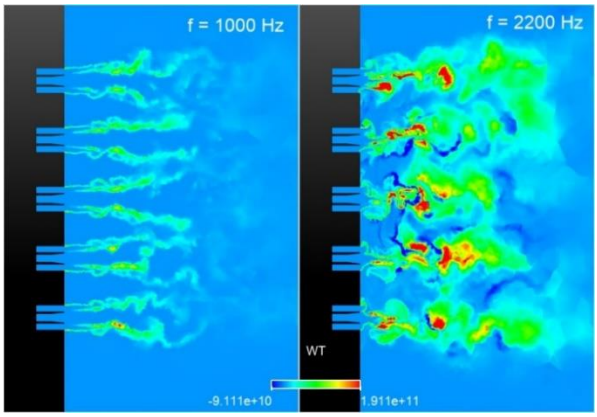

Figure 23. Instantaneous heat release field with a modulation of 1000 Hz (left) and 2200 Hz (right).

To quantify the influence of pressure modulation, the heat release ω_T is integrated on a slice of the chamber as shown in Figure 25 and the evolution of this integral is plotted as a function of z/D_l in Figure 26. Acoustic modulation increases the combustion efficiency, the green curve (Modulated case: MC) being systematically above the blue one (Non Modulated case: NMC). The heat release peak is located much earlier in the chamber and is more intense and narrower. Similar results have been found in the supercritical regime [27] in the case of flow oscillations.

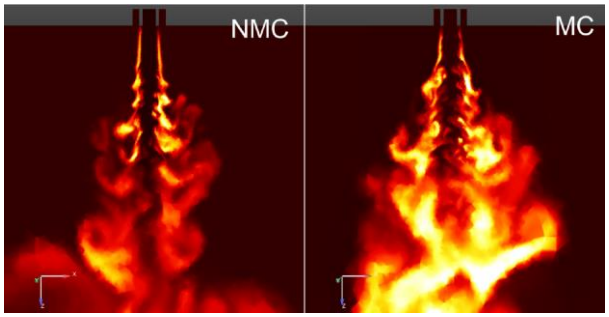

Figure 24. Instantaneous temperature field without modulation NMC (left) and with modulation MC (right)

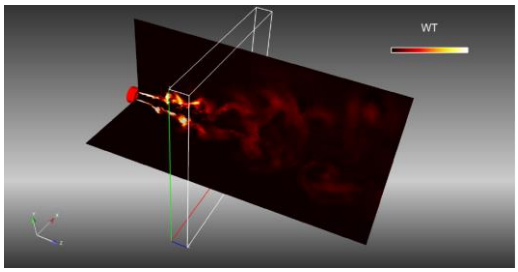

Figure 25. Slice for hear release integration

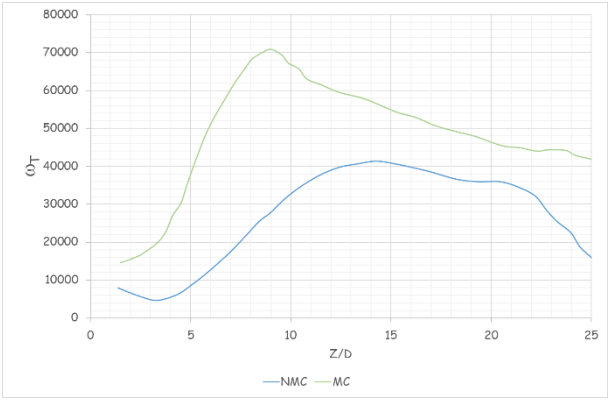

Figure 26. Evolution in the chamber of the heat release integral for modulated case (MC) and non modulated case (NMC)

6. CONCLUSION

The study presented in this paper allowed to set up all the tools for the simulation of a firing test on the MASCOTTE bench equipped with the VHAM device in subcritical conditions and to carry out first attempt computations with acoustic modulation. First, a simulation of the case without modulation was performed on a coarse mesh in order to serve as an initial condition for the modulated case. For this steady-state case, the length of the liquid core for the injectors is correct with respect to the different correlations available in the literature. The five flames have similar behaviour. Moreover, as the flames burn with low temperatures, a further study was carried out on numerical experiment with similar condition to the VHAM test case. This case is a mono-injector set in an intensity anti-node. Thus, we were able to demonstrate that the choices of spatial discretization and turbulence injection allow a more realistic flow to be obtained, and the cost of such choices could be evaluated. These parameters nevertheless have a limited role on the temperature in the mixing layer under combustion conditions. The atomization model also has a particularly important role in the cascade of phenomena and models used. It has been shown to be the phenomenon limiting combustion, and further investigations on modelling this cascade are required to be able to retrieve realistic flame characteristics.

Then, a methodology was implemented for the simulation of the VHAM system and its effectiveness was demonstrated. Finally, it was used to carry out two modulated simulations on a coarse mesh. Thus, for the two cases, a shortening of the liquid core was highlighted, this shortening being partly due to the inflow oscillations induced by the pressure modulation. This decrease in size is, however, much greater when the modulation corresponds to an eigenmode of the chamber. It is also in this case that the coupling between combustion and acoustics is strengthened and the response of the chamber pressure is maximized. Like for the steady-state investigation, the influence of the acoustic modulation was studied in detail on the single injector test case. It confirmed the reduction in the size of the liquid core as well as its flattening and showed a strengthening of the combustion and a widening of the flame.

This paper has laid a solid and indispensable foundation for the numerical simulation of a semi-industrial case of high frequency combustion instabilities under subcritical injection conditions. It also showed the important impact of liquid phase modelling on combustion. The next step will be to carry out the simulation on a finer mesh with adapted atomization and turbulence models. This simulation will be compared with the experimental results.

Acknowledgments

The generous support of CNES is gratefully acknowledged.

7. REFERENCES

1. Sutton, G. P. & Biblarz, O. (2016). Rocket propulsion elements. *John Wiley & Sons.*
2. Culick, F.E. (2006) Unsteady motions in combustion chambers for propulsion systems. *AGARDograph, Technical Report*, NATO/RTO-AG-AVT-039.
3. Anderson, W. & Yang, V. (1995). Overview of combustion instabilities in liquid-propellant rocket engines, liquid rocket engine combustion instability. *Progress in Astronautics and Aeronautics,* **Vol 169**, pp.3-37.
4. Jensen R.J. and al. (1989) LOX/Hydrocarbon combustion instability investigation *NASA contract NAS3-24612, NASA CR-182249,* Rocketdyne (1989)

5. Breisacher K., Priem R.J.(1990). Analysis of 5kHz combustion instabilities in 40K Methane/LOX combustion chambers. *NASA TM 101368*
6. Habiballah, M., Orain, M., Grisch, F., Vingert, L. & Gicquel P. (2006). Experimental studies of high-pressure cryogenic flames on the MASCOTTE facility, *Combustion Science and Technology Journal*, **Vol 178**, numer 1-3, pp.101-128.
7. ReflochA., Courbet B., Murrone A., Villedieu P., Laurent C., Gilbank P., Troyes J., Tessé L., Chaineray G., Dargaud J.B., Quémerais E. & Vuillot F. (2011). CEDRE Software. *Aerospace Lab*, vol. 2.
8. Mery Y., Hakim L., Scouflaire P., Vingert L., Ducruix S. and Candel S.(2013). Experimental Investigation of Cryogenic Flame Dynamics under Transverse Acoustic Modulations *Comptes Rendus Mecanique* 341 pp. 100-109.
9. Hakim, L., Schmitt, T., Ducruix, S. & Candel, S. (2015) Dynamics of a transcritical coaxial flame under a high-frequency transverse acoustic forcing: Influence of the modulation frequency on the flame response. *Combustion and Flame* 162(10), pp. 3482-3502
10. Le Touze, C. Dorey, L.-H. Rutard, N. & Murrone, A. (2020). A compressible two-phase flow framework for Large Eddy Simulations of liquid-propellant rocket engines, *Applied Mathematical Modelling*, Volume 84, Pages 265-286
11. Rutard, N., Dorey, L-H., Le Touze C. & Ducruix, S. (2020). Large-eddy simulation of an air-assisted liquid jet under a high-frequency transverse acoustic forcing, *International Journal of Multiphase Flow*, Volume 122, 2020, 103144,ISSN 0301-9322
12. Eroglu, H., Chigier, N. & Farago., Z. (1991). Coaxial atomizer liquid intact lengths. Physics of Fluids A : Fluid Dynamics 3, 303
13. Villermaux, E. (1998). Mixing and Spray Formation in Coaxial Jets. *Journal of Propulsion and Power* Volume 14, N°5
14. Leroux, B., Delabroy, O. & Lacas, F. (2007). Experimental Study of Coaxial Atomizers Scaling. Part I : *Dense Core Zone.* Atomization and Sprays 17(5):381-407
15. Gaillard, P., Le Touze, C., Matuszewski, L. & Murrone, A., (2016). Numerical Simulation of Cryogenic Injection in Rocket Engine Combustion Chambers. *AerospaceLab*, pp.16
16. Smagorinsky, J. S. (1963). General Circulation Experiments with the Primitive Equations: I. The basic Experiment. *Monthly Weather Revue*, vol. 91, nº 3, p. 99-164
17. Le Touze, C., Murrone, A. & Montreuil, E. (2013). Numerical coupling strategies for the "separated-to-dispersed" transition within the liquid phase of cryogenic rocket engines. 5th *European Conference For Aeronautics and Space Sciences*
18. Toro, E.F., Spruce, M. & Speares, W. (1994). Restoration of the contact surface in the HLL-Riemann solver. *Shock Waves*, 4(1):25–34.
19. Le Touze, C., Murrone, A. & Guillard, H. (2014) Multislope MUSCL method for general unstructured meshes. *Journal of Computational Physics* RR-8463, pp.40.
20. Spalding, D. (1971). Mixing and chemical reaction in steady confined turbulent flames. *Symposium International on Combustion* 13:1 649–657.
21. Magnussen, B. & Hjertager, B. (1977). On mathematical modeling of turbulent combustion with special emphasis on soot formation and combustion. *Symposium International on Combustion* 16:1, 719–729.
22. Schmitt, T. (2020). Large-Eddy Simulations of the Mascotte Test Cases Operating at Supercritical Pressure. *Flow Turbulence Combust* **105,** 159–189.
23. Le Touze. C. (2015). Couplage entre modèles diphasiques à « phases séparées » et à « phase dispersée » pour la simulation de l'atomization primaire en combustion cryotechnique. *PhD Thesis* Université Nice Sophia Antipolis.
24. Goodwin, D.G. Speth, R.L. Moffat, H.K. & Weber, B.W. (2018) *Cantera: An object-oriented software toolkit for chemical kinetics, thermodynamics, and transport processes*. https://www.cantera.org.
25. Jarrin, N. Prosser, R. Uribe, J.-C. Benhamadouche, S. & Laurence, D. (2009) A Reconstruction of turbulent fluctuations for hybrid RANS/LES simulations using a synthetic-eddymethod, *International Journal of Heat and Fluid FLow*, 30, pp. 435–442.
26. Mery, Y. (2010). High-Frequency Combustion Instability Mechanisms and Application to Rocket Engines *PhD Thesis* de docteur en énergétique du laboratoire d'Energétique Moléculaire et Macroscopique, Combustion (EM2C) du CNRS et de l'ECP
27. Nez, R. Schmitt, T. & Ducruix, S. (2018) High-Frequency Combustion Instabilities in Liquid Rocket Engines Driven by Propellants Flow Rate Oscillations. *3AF SpacePropulsion Conference*, May 2018, Seville, Spain.